Proceedings of the ASME 2022 Fluids Engineering Division Summer Meeting
FEDSM2022
August 3 – August 5, 2022, Toronto, Ontario, Canada

FEDSM2022- 85407

A BALANCE BETWEEN ODOR INTENSITY AND ODOR PERCEPTION RANGE IN ODOR-GUIDED FLAPPING FLIGHT

Menglong Lei and Chengyu Li

Department of Mechanical Engineering, Villanova University, Villanova, PA 19085

ABSTRACT

Insects rely on their olfactory system to forage, prey, and mate. They can sense odorant plumes emitted from sources of their interests with their bilateral odorant antennae, and track down odor sources using their highly efficient flapping-wing mechanism. The odor-tracking process typically consists of two distinct behaviors: surging upwind at higher velocity and zigzagging crosswind at lower velocity. Despite extensive numerical and experimental studies on odor guided flight in insects, we have limited understandings on the effects of flight velocity on odor plume structure and its associated odor perception. In this study, a fully coupled three-way numerical solver is developed, which solves the 3D Navier-Stokes equations coupled with equations of motion for the passive flapping wings, and the odorant convection-diffusion equation. This numerical solver is applied to resolve the unsteady flow field and the odor plume transport for a fruit fly model at different flight velocities in terms of reduced frequency. Our results show that the odor plume structure and intensity are strong related to reduced frequency. At smaller reduced frequency (larger forward velocity), odor plume is pushed up during downstroke and draw back during upstroke. At larger reduced frequency (smaller forward velocity), the flapping wings induce a shield-like air flow around the antennae which may greatly increase the odor sampling range. Our finding may explain why flight velocity is important in odor guided flight.

NOMENCLATURE

A_ϕ	: Stroke angle amplitude
b	: Wing spanwise length
$\bar{c}$	: Mean wing chord length
C	: Odor intensity
C^*	: Non-dimensional odor intensity
Ch	: Cauchy number
C_L	: Lift coefficient
f	: Flapping frequency
G	: Torsional stiffness of the spring
I	: Moment of inertia
M_{aero}	: Moment due to the aerodynamic force
$M_{elastic}$	: Moment due to the elastic force
$M_{gravity}$	: Moment due to the gravitational force
Re	: Reynolds number
S	: Wing surface area
u_i	: Velocity component
U_i	: Face-centered velocity component
$\bar{U}_{tip}$	: Averaged wing tip velocity
α	: Odor diffusivity
ϕ	: Wing stroke angle
θ	: Wing pitch angle
θ_0	: Rest angle
ω	: Angular velocity
ρ_{air}	: Fluid density
ν	: Kinematic viscosity

INTRODUCTION

Airborne insects are capable of sensing and tracking down odor plumes of their interest emitted from sources beyond their visual range. These olfactory cues are odorants generally characterized by filamentous odor plumes segmented by low or zero concentration blanks. Recent progresses on insect neuronal mechanisms discovered that that insects are capable of resolving fast olfaction dynamics[1, 2] and odor concentration gradient between their odor receptors [3]. This enables insects to detect the odor concentration variations in both time and space. However, since the locomotion of insects requires significant amount of energy to sustain constant wing flapping motion even during hovering, insects must extract sufficient information from the odorant receptors during limited time.

Van Breugel et al [4] studied the odor tracking behaviors of fruit flies in a wind tunnel and described the two specific behaviors while encountering odor plume. Fruit flies zigzag crosswind at lower velocity to upwind when encountering and losing an odor plume. When they sense the odor plume again, they surge upwind at higher velocity to visual stimulus [5]. It is true that fruit flies zigzag crosswind through the odor landscape to actively enhance odor filament detection range. Meanwhile, their flapping wings alter both the aerodynamics and the velocities in the flow field, which further complicates the odor landscape. The question is, what is the role of the flight velocity in odor guided flight?

To answer this question, the odor landscape must be visualized. However, most previous studies on odor plume structures during odor-guided flight of insects are limited on experimental observation. The lack of quantitative measurement method of odor intensity at small length scale makes it hard to understand the effects of flapping wings and flight velocity on odor landscape. In addition to experimental measurements, numerical simulation, as an alternative approach to obtain the instantaneous odor landscape, is also limited in literature. One of the challenges is to solve the odor advection-diffusion equation based on the instantaneous velocity field during odor guided flight. In recent studies, Li et al. [6-8] and Lei et al. [9] included the flapping wing kinematics in their simulations and visualized the odor plume structure of a fruit fly model in forward flight. They confirmed that the antennae are well positioned to perceive the odor plume while avoiding wing-induced disturbance. Nevertheless, the Lagrange particle tracing approach used in their studies failed to consider the diffusion in the odorant transport. To date, it is still unclear how the odor plume structure is perturbed by flight velocity and wing-induced flow.

In this paper, direct numerical simulations were conducted to investigate odor plume structures that are modified by the flight velocity and wing flapping kinematics. In order to mimic the odor-tracking flights, an odor source was placed in front of the fruit fly model in the upstream. The effects of flight velocity is investigated in terms of reduced frequency by changing the incoming air velocity. For the flapping wings, the wing pitch motion was simulated based on the aerodynamic loading using a torsional spring model. All simulations were conducted using an in-house three-dimensional immersed-boundary-method-based computational fluid dynamics (CFD) solver in which the Navier-Stokes equations and the equations of motion for passive pitching wings were couple together to obtain the flow field. The odor convection-diffusion equation was then solved at each time step to resolve the odor concentration field.

METHODOLOGY

Governing equations and numerical method

The three-dimensional viscous incompressible Navier-Stokes equations are solved using an in-house immersed-boundary-method based CFD solver. The equations are written in tensor form:

$$\begin{cases} \dfrac{\partial u_i}{\partial x_i} = 0 \\ \dfrac{\partial u_i}{\partial t} + \dfrac{\partial \left(u_i u_j\right)}{\partial x_j} = -\dfrac{1}{\rho}\dfrac{\partial P}{\partial x_i} + \nu \dfrac{\partial}{\partial x_j}\left(\dfrac{\partial u_i}{\partial x_j}\right) \end{cases} \tag{1}$$

Where u_i are the velocity component, P is the pressure, ρ is the fluid density, ν is the kinematic viscosity.

The above equations are discretized using a cell-centered, collocated arrangement of the primitive variables, and are solved using a finite difference-based immersed-boundary method [10] in a non-body-conforming Cartesian grid. The equations are integrated with time using the fractional step method. Details of the CFD solver in solving Navier–Stokes equations is elaborated and validated in our previous studies [11-13]. The CFD solver has been successfully applied to study canonical revolving wings [14-17], flapping propulsion problems [12, 18-21], insect flight [7, 8, 13, 22, 23], and human nasal airflow [24, 25].

Based on the resolved velocity field by solving the Navier-Stokes equations, we then solve the odorant advection-diffusion equation:

$$\frac{\partial C}{\partial t} + \frac{\partial C U_i}{\partial x_i} = D\frac{\partial^2 C}{\partial x_i^2} \tag{2}$$

Where C is the odor intensity, D is the odor diffusivity, U_i is the face-centered velocity obtained from interpolation of the cell-centered velocity u_i. The equation is discretized using an implicit method:

$$\frac{C^{n+1} - C^n}{\Delta t} + \frac{\delta C^n U_i^n}{\delta x_i} = D\frac{\delta}{\delta x_i}\left(\frac{\delta C^{n+1}}{\delta x_i}\right) \tag{3}$$

The Navier–Stokes equations and odor convection-diffusion equation are discretized on non-body-conforming Cartesian grid, thus eliminates the complex re-meshing algorithms for moving boundaries on body-conforming grids at each time step. The differential equation for odor transportation can be written as

$$\begin{aligned} &C_P^{n+1} - \alpha\Delta t\left(a_W C_W^{n+1} + a_E C_E^{n+1} + a_N C_N^{n+1} + a_S C_S^{n+1} + a_B C_B^{n+1} + a_F C_F^{n+1} + a_P C_P^{n+1}\right) \\ &\quad = C_P^n - \Delta t\left(\frac{C_e^n U_e^n - C_w^n U_w^n}{\Delta x} + \frac{C_n^n U_n^n - C_s^n U_s^n}{\Delta y} + \frac{C_f^n U_f^n - C_b^n U_b^n}{\Delta z}\right) \end{aligned} \tag{4}$$

Where the coefficients a_W, a_E, a_N, a_S, a_B, a_F, a_P are calculated by discretizing the diffusion term

$$\frac{\delta}{\delta x_i}\left(\frac{\delta C}{\delta x_i}\right)=\frac{\frac{C_E-C_P}{\Delta x}-\frac{C_P-C_W}{\Delta x}}{\Delta x}+\frac{\frac{C_N-C_P}{\Delta y}-\frac{C_P-C_S}{\Delta y}}{\Delta y}+\frac{\frac{C_F-C_P}{\Delta z}-\frac{C_P-C_B}{\Delta z}}{\Delta z} \quad (5)$$
$$=a_E C_E+a_W C_W+a_N C_N+a_S C_S+a_F C_F+a_B C_B+a_P C_P$$

The uppercase letters W, E, N, and S represent cell-centered variables, and the lowercase letters w, e, n, and s represent face-centered variables which are calculated by interpolation of the corresponding cell-centered variables.

This approach has been successfully applied to investigate the odor plume structure perturbed by canonical pitching-plunging motion[26] and flapping wings of insects[27].

Wing model with torsional spring

The fruit fly model adopted here has been used in our previous studies [8, 9]. The aspect ratio of the wing is 3.2, defined as $(\text{span})^2/(\text{area})$. As shown in Figure 1 (a), the kinematics of the wing is defined by three Euler angles, stroke (ϕ), deviation (ψ), and pitch (θ) angle. In Figure 1 (b), the stroke plane angle β is 20°, the incline angle χ is 45°. As the wing flaps back and forth in the stroke plane with a prescribed stroke angle (ϕ) and the wing root acting like a torsional spring, the wing pitches passively about wing leading edge.

The wing stroke angle is defined in equation (6), while the wing deviation angle is fixed as zero during the entire flapping motion.

$$\phi(t)=-A_\phi\cos(2\pi f t) \quad (6)$$

Where $\phi(t)$ is the instantaneous wing stroke angle at time t, A_ϕ = 140° is the stroke amplitude, and f is the flapping frequency.

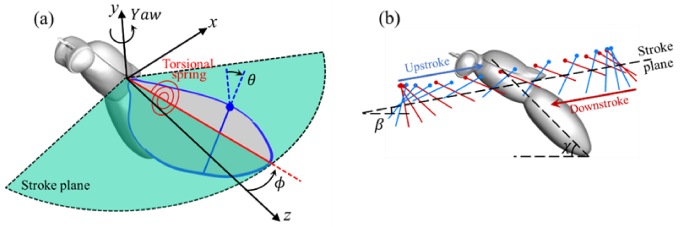

Figure 1. Schematic of the flapping wing with a torsional spring (a) and wing chord diagram during upstroke and downstroke. Where θ is the pitch angle, ϕ is the stroke angle, β is the stroke plane angle, χ is the body incline angle.

By calculating the aerodynamic, elastic, and inertial forces at each time step, the passive wing pitch angle (θ) is calculated using a torsional spring model, in which the wing root is represented by a torsional spring. The angular velocity of pitch angle is then calculated by solving the equations of motion, which can be written as follows

$$I_{xx}\dot{\omega}_x+\left(I_{zz}-I_{yy}\right)\omega_y\omega_z+I_{xy}\left(\omega_x\omega_z-\dot{\omega}_y\right)+I_{yz}\left(\omega_z^2-\omega_y^2\right)$$
$$-I_{xz}\left(\dot{\omega}_z+\omega_x\omega_y\right)=M_{aero}+M_{elastic}+M_{gravity} \quad (8)$$

Where I_{xx}, I_{yy}, I_{zz}, I_{xy}, I_{xx}, and I_{xz} are momentum of inertia of the wing. M_{aero}, $M_{elastic}$, and $M_{gravity}$ are the momentum due to aerodynamic, elastic, and gravitational forces, respectively.

The nondimensional torsional stiffness of the wing root is indicated by the Cauchy number Ch [28] defined as the ratio of the fluid dynamic pressure force to the structure elastic force, which can be expressed as follows:

$$Ch=\frac{\rho_{air}A_\phi^{\,2}f^2\bar{c}^3b^2}{G} \quad (9)$$

Where $\bar{c}$ is the mean wing chord length, b is the wing spanwise length. The Cauchy number Ch selected in this paper is 0.27 based on our previous study [29, 30]. At which both the lift and power coefficient are optimized.

At each time step, the Navier–Stokes equations for the fluid field and the equations of motion for solid wings are coupled and solved using an implicit method. The location and angular velocity of the wing is then updated from the previous time step. The aerodynamic forces are obtained by integrating the pressure and shear on the surface of the insect.

Simulation setup

Fruit flies zigzag crosswind at lower velocity when searching for odor plumes and surge upwind at high velocity when they detect an odor plume. To interpret how the forward flight velocity affects the sensitivity of odor plumes on the antennae, the effects of forward flight velocity in terms of reduced frequency $k = fb/U_\infty$ are investigated within the range from 0.325 to 1.5. The corresponding range of real forward velocity is 0.47 ~ 1.87 m/s. As shown in Figure 2, an odor source is placed in front of the fruit fly at constant odor concentration C_0. At the other boundaries, the odor concentration is 0.

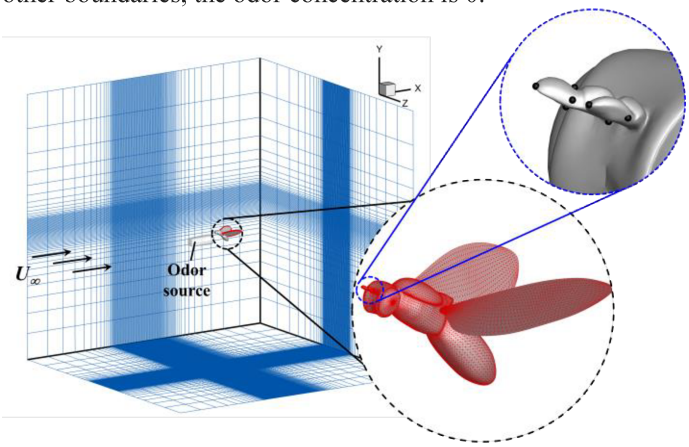

Figure 2. Simulation setup and computational grids applied in the study. An odor source is placed in front of the fruit fly with odor intensity of 1. On each of the two probes of the fruit fly, the average value of five points is used to represent the probe. The simulation is performed in a 10 million size non-

uniform Cartesian grid. The body and wings are represented by high-density unstructured triangular surface mesh.

The odorant transport phenomenon is characterized by two non-dimensional parameters, Reynolds number (Re) and Schmidt number (Sc). The Reynolds number is defined as $\mathrm{Re} = \bar{U}_{tip} b / \nu$, where $\bar{U}_{tip}$ is the average wingtip velocity. The current setup result in a Reynolds number of 180 which is in line with real fruit fly data[31]. Schmidt number Sc is the ratio between kinematic viscosity and odor diffusivity ($\mathrm{Sc} = \nu / D$), which can be used to characterize fluid flows in which there are simultaneous momentum and mass diffusion convection processes. Small Sc indicates odor diffusion dominant the odor transportation, while large Sc indicates odor convection dominant the odor transportation.

The simulations were performed in a non-uniform Cartesian grid. The computational domain size of the simulation is $30\bar{c} \times 30\bar{c} \times 30\bar{c}$ in terms of mean wing chord length ($\bar{c}$). The grid size used in the current study is 320×128×240. As shown in Figure 2, the domain mesh has two refined layers. A high resolution in a cuboidal region around the insect is provided with the smallest resolution. Around this region, there is a secondary denser layer. Beyond the secondary denser layer, there is coarse stretched layer. Boundary conditions on all walls of the computational domain are set as Neumann boundary condition except Dirichlet boundary condition is set on the inlet wall with constant incoming velocity and odor intensity. The fruit fly body and wings are represented by high-density triangular surface mesh. The odor intensity around antennae is measured using virtual probes. Five virtual points at different locations around each antenna are selected. At each time step, the odor intensity on the 5 points is recorded.

RESULTS

The time history of aerodynamic performance, lift coefficient C_L ($C_L = 2F_L / \left(\rho \bar{U}_{tip}^2 S\right)$), drag coefficient C_D ($C_D = 2F_D / \left(\rho \bar{U}_{tip}^2 S\right)$), passive pitch angle θ, and normalized odor concentration C^* ($C^* = C / C_0$) of the fruit fly at different k are plotted in Figure 3, where F_L, F_D, and S are lift, drag, and wing surface area, respectively. Note that smaller k indicates larger forward velocity. As k increases, we see that the flapping wings generate larger aerodynamic forces (lift and drag) during upstroke. While during downstroke, the wings generate smaller aerodynamic forces. The cycle-averaged $\bar{C}_L$ decrease with k. As for the drag, since we kept the same stroke plane angle for all the cases, at smaller k (larger forward velocity), the flapping wings generate positive drag force. At larger k (smaller forward velocity), the flapping wings generate nagetive drag force (thrust). The pitch angle θ is calculated using the torsional spring model elaborated in section 2.2 which includes the aerodynamic forces, elastic forces, and momentum forces on the wing. Since the aerodynamic force is smaller at larger k, the cycle-averaged pitch angle $\bar{\theta}$ also decreases with k.

Figure 3 (d) presents the odor sensitivity on the antennae for different k. Under current setup, we see that the odor sensitivity on the antennae is larger for smaller k (0.325 ~ 0.65), at which the forward velocity is larger. While at larger k (0.919 ~ 1.3), the odor sensitivity is much smaller. Another noticeable difference is that at smaller k, the odor sensitivity is maximized during upstroke and minimized during downstroke. While at larger k, the odor sensitivity shows an opposite trend. This observation can be further explained using the streaklines shown in Figure 7. In general, larger k denotes stronger wing-induced flow. At k = 0.325 (Figure 7 (a1~a4)), the incoming air velocity is the strongest that the wing-induced flow can hardly affect the flow field before the antennae. As k increases to 0.65 (Figure 7 (b1~b4)), the wing-induced flow pushes odor plume up to the antennae region. However, at k = 1.3, the wing-induced flow is the strongest, which creates a shield-like air flow circling around the insect and prevent the antennae from detecting the odor plume. The antennae in this case can no longer sense the odorant released from the upstream but rather the odorants induced by the wings. The odor sensitivity is not only undermined, but the peak value of odor concentration occurs at mid-downstroke when the bilateral wings flaps forward to the thorax.

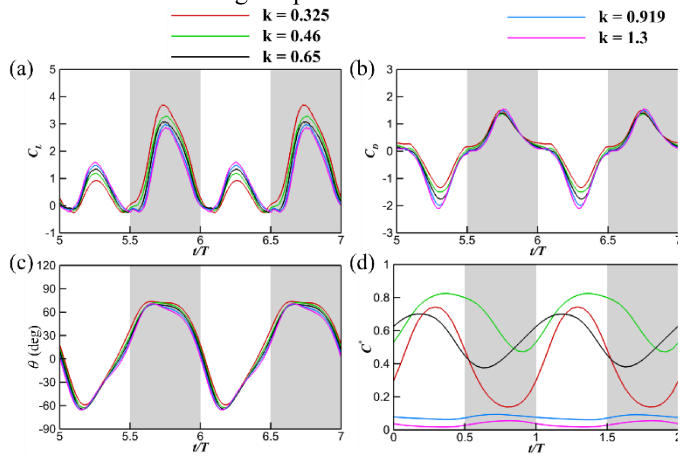

Figure 3. Time history of lift coefficient C_L (a), drag coefficient C_D (b), pitch angle θ (c), and normalized odor concentration C^* (d) for different reduced frequency k ranging from 0.325 to 1.3.

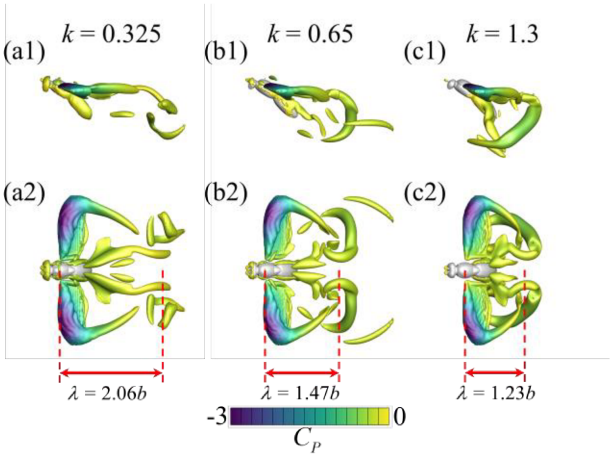

Figure 4. Sideview and topview of wake topology visualized by plotting iso-surface of Q-criterion at mid-downstroke for reduced frequency k = 0.325 (a1) and (a2), 0.65 (b1) and (b2), and 1.3 (c1) and (c2). The wake topologies are colored by pressure coefficient.

Figure 4 presents the wake topology colored by pressure coefficient $C_P = 2(P - P_\infty)/\rho U_\infty^2$ for different k at mid-downstroke. At smaller k, the larger incoming air velocity generates stronger wingtip vortex and trailing edge vortex that shed downstream. As k increases, the strength and size of wingtip vortex and trailing edge vortex decrease, while the vortices shed during upstroke are more discernable. Meanwhile, the wingtip vortex, trailing edge vortex, and vortices generated during upstroke, together merge and form an interconnected vortex ring.

Figure 5 shows the time-averaged normalized odor concentration C^* on the antennae for different k. The fruit flies are colored by odor concentration to provide a comprehensive understanding of odor plume structure on the surface. Under current setup, at k = 0.46, the odor sensitivity on the antennae reaches to its maximum. As k continues to increase, the odor sensitivity decreases. To explain this phenomenon, we extracted the instantaneous odor plume structure on the symmetry plane.

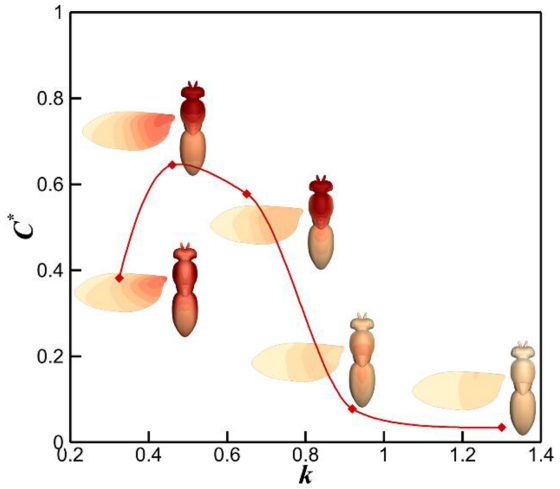

Figure 5. Time-averaged normalized odor concentration C^* on the antennae for different k. The fruit flies colored by C^*.

Figure 6 presents the normalized odor concentration C^* contour on the symmetry plane at t/T = 0, 0.25, 0.5, and 0.75 for different k. At k = 0.325 (a1~a4) and 0.65 (b1~b4), the incoming air flow dominates the flow field. We see the odor plume remains intact near the antennae region. The odor plume is draw downward during upstroke and pushed upward during downstroke by the wing-induced flow. Thus the odor sensitivity is maximized during upstroke and minimized during downstroke. However, as k increases to 1.3, the incoming air flow is the smallest and wing-induced flow dominates the flow around the antennae. During upstroke, we see that an odor filament before the thorax forms at mid-upstroke and reaches the antennae at mid-downstroke. The odor sensitivity at k = 1.3 is thus maximized during downstroke and minimized during upstroke. For all three reduced frequencies, not only a higher velocity region is situated around the antennae, but the odor concentration is significantly higher than other part of the body (Figure 5). This could further prove that the antennae are well located where they can best sense the odorants. While other part of the insect body, e.g., dorsal region, although the odor concentration may be high, the low velocity and longer distance may delay odor perception timing and undermine temporal resolution in odor perception.

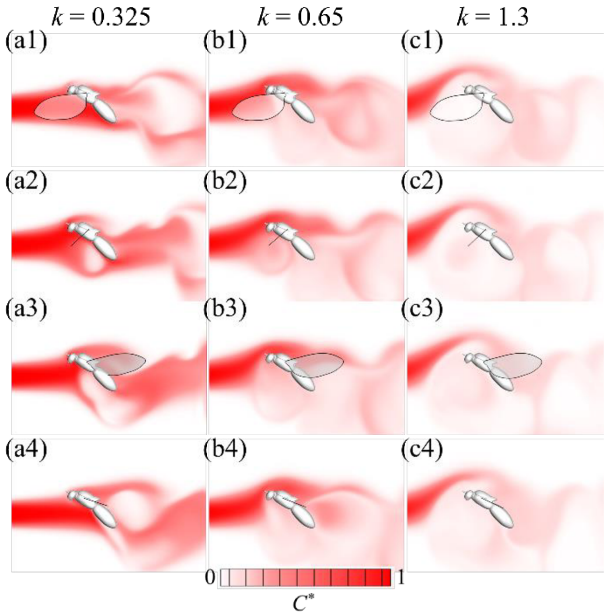

Figure 6. Normalized odor concentration C^* contour on the symmetry plane at t/T = 0, 0.25, 0.5, and 0.75 for k = 0.325 (a1~a4), 0.65 (b1~b4), and 1.3 (c1~c4).

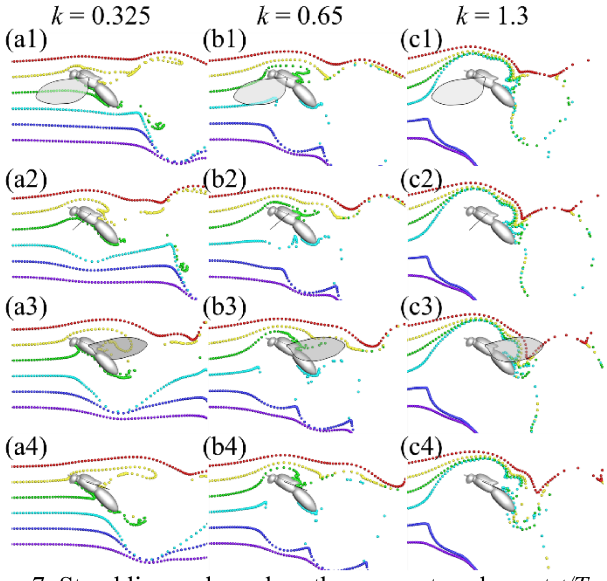

Figure 7. Streaklines released on the symmetry plane at t/T = 0, 0.25, 0.5, and 0.75 for k = 0.325 (a1~a4), 0.65 (b1~b4), and 1.3 (c1~c4).

Streaklines released on the symmetry plane are also presented in Figure 7 for different k. Using Lagrangian tracking approach, we are able to calculate the locomotion of these particles and visualized the transport of odor filaments released at certain locations. The streaklines exhibit the same trend in odor concentration contour. At large k, the streaklines released in front of the fruit fly can not reach the antennae. To investigate where the odorants on the antennae come from, we calculated the initial locations of odorants that reach the antennae region using backward Lagrangian tracking approach, as shown in Figure 8.

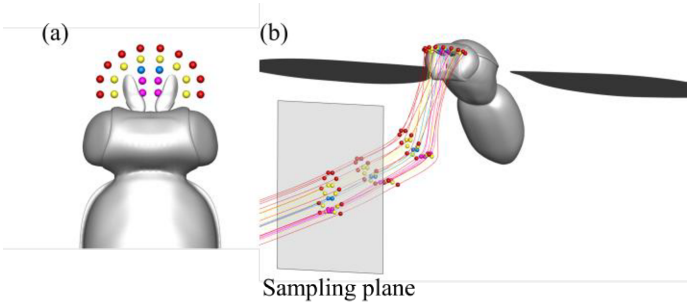

Figure 8. Schematics of the backward Lagrangian tracking approach. (a) release locations of the tracked particles near the antennae and (b) calculations of the initial locations of these particles on the sampling plane. By reversing time and velocity, trajectory of particles are tracked backward to the upstream flow field using Lagrangian approach.

We first release particles continuously near the antennae, as shown in Figure 8 (a). Using the saved instantaneous data, by reversing time and velocity, we are able to track the particles backward to the upstream flow field. The velocity and position of particles are interpolated and calculated using 4th order Runge-Kutta method, as shown in Figure 8 (b). The calculation results of the initial locations are shown in Figure 9. At small k (Figure 9 (a)), the initial locations are centered in front of the antennae. As k increases (Figure 9 (b)), the incoming velocity decreases, the wing induced flow starts to dominant the flow field. We see that the initial locations move downward, but still centered near the symmetry plane. At $k = 1.3$ (Figure 9 (c)), the initial locations disperse widely across the sampling plane, but the high concentration region is located even lower. Note that few of the initial locations in this case are centered near the symmetry plane, which means that the antennae can sense odorants not directly from its front, but from a much wider area.

Figure 10 summarizes the outlines that cover the initial locations of particles that may reaches the antennae. As k increases, we see that not only the outlines move downward, but the area of the outlines increases. As k increases, the wing-induced flow dominates the flows around the insect. As a result, odorants from larger area can be induced to the antennae, the insect can now perceive larger area of odor plumes. However, as previously mentioned in Figure 6 (c1~c4), the sensitivity at large k can be greatly decreased if the insect is tracking a specific odor plume. Our findings can explain the two behaviors in odor-guided flight that insects zigzag crosswind at lower velocity when in search of an odor plume and surge upwind at higher velocity when an odor plume is detected.

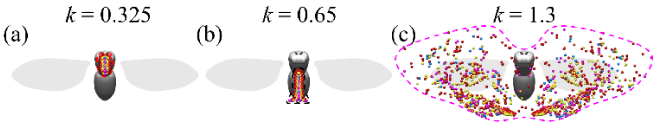

Figure 9. Initial locations of particles that flow into the antennae region calculated using backward Lagrangian tracking approach for different k. The dashed lines denote the bulk of the initial locations.

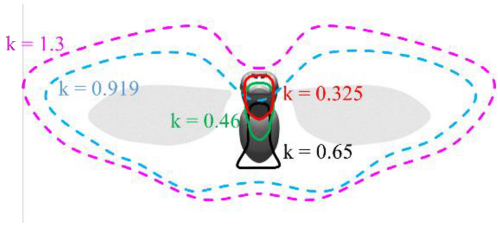

Figure 10. Overlaped dashed lines that cover the bulk of the initial locations for different k.

CONCLUSIONS

The aerodynamic performance and odor intensity for different reduced frequency during odor tracking flight were investigated by solving the 3D Navier-Stokes equations, coupled with equations of motion for the passive pitching wings, and the convection-diffusion equation for the odor transportation. The odor perception time and intensity are strong related to reduced frequency. At smaller reduced frequency (larger forward velocity), odor plume is pushed up above the antennae during downstroke and draw back to the antennae during upstroke. Thus odor sensitivity is maximized during downstroke and minimized during upstroke. At larger reduced frequency (smaller forward velocity), the flapping wings induce a shield-like air flow that prevents the antennae from sensing odorants advected directly from its front. However, the antennae are thus able to sense odor plumes in a much larger area range. This finding may explain why insects fly surge upwind at higher velocity when tracking down an odor plume and zigzag at lower velocity when searching for odor plume.

ACKNOWLEDGMENTS

This research was supported by the National Science Foundation (CBET-2042368) to C. Li. All simulations were run on the High-Performance Computing Cluster of the College of Engineering at Villanova University.

REFERENCES

[1] A. Egea-Weiss, A. Renner, C. J. Kleineidam, and P. Szyszka, "High precision of spike timing across olfactory receptor neurons allows rapid odor coding in Drosophila," *IScience,* vol. 4, pp. 76-83, 2018.

[2] P. Szyszka, R. C. Gerkin, C. G. Galizia, and B. H. Smith, "High-speed odor transduction and pulse tracking by insect olfactory receptor neurons," *Proceedings of the National Academy of Sciences,* vol. 111, pp. 16925-16930, 2014.

[3] B. J. Duistermars, D. M. Chow, and M. A. Frye, "Flies require bilateral sensory input to track odor gradients in flight," *Current Biology,* vol. 19, pp. 1301-1307, 2009.

[4] F. van Breugel and M. H. Dickinson, "Plume-tracking behavior of flying Drosophila emerges from a set of distinct sensory-motor reflexes," *Current Biology,* vol. 24, pp. 274-286, 2014.

[5] I. Balásházy, W. Hofmann, Á. Farkas, and B. G. Madas, "Three-dimensional model for aerosol transport and deposition in expanding and contracting alveoli," *Inhalation toxicology,* vol. 20, pp. 611-621, 2008.

[6] C. Li, "Effects of wing pitch kinematics on both aerodynamic and olfactory functions in an upwind surge," *Proceedings of the Institution of Mechanical Engineers, Part C: Journal of Mechanical Engineering Science,* vol. 235, pp. 296-307, 2021.

[7] C. Li, H. Dong, and K. Zhao, "Dual functions of insect wings in an odor-guided aeronautic navigation," *Journal of fluids engineering,* vol. 142, p. 030902, 2020.

[8] C. Li, H. Dong, and K. Zhao, "A balance between aerodynamic and olfactory performance during flight in Drosophila," *Nature communications,* vol. 9, pp. 1-8, 2018.

[9] M. Lei and C. Li, "Numerical investigation of the passive pitching mechanism in odor-tracking flights," *AIAA paper 2020-3016,* 2020.

[10] H. Wan, H. Dong, and G. P. Huang, "Hovering hinge-connected flapping plate with passive deflection," *AIAA journal,* vol. 50, pp. 2020-2027, 2012.

[11] R. Mittal, H. Dong, M. Bozkurttas, F. Najjar, A. Vargas, and A. Von Loebbecke, "A versatile sharp interface immersed boundary method for incompressible flows with complex boundaries," *Journal of computational physics,* vol. 227, pp. 4825-4852, 2008.

[12] C. Li, H. Dong, and G. Liu, "Effects of a dynamic trailing-edge flap on the aerodynamic performance and flow structures in hovering flight," *Journal of Fluids and Structures,* vol. 58, pp. 49-65, 2015.

[13] C. Li and H. Dong, "Wing kinematics measurement and aerodynamics of a dragonfly in turning flight," *Bioinspiration & Biomimetics,* vol. 12, p. 026001, 2017.

[14] C. Li, H. Dong, and B. Cheng, "Effects of aspect ratio and angle of attack on tip vortex structures and aerodynamic performance for rotating flat plates," *AIAA 2017-3645,* p. 3645, 2017.

[15] H. Wan, H. Dong, C. Li, and Z. Liang, "Vortex Formation and Aerodynamic Force of Low Aspect-Ratio Plate in Translation and Rotation," *AIAA Paper 2012-3278,* 2012.

[16] C. Li, H. Dong, and B. Cheng, "Tip vortices formation and evolution of rotating wings at low Reynolds numbers," *Physics of Fluids,* vol. 32, p. 021905, 2020.

[17] J. Wang, C. Li, R. Zhu, G. Liu, and H. Dong, "Wake structure and aerodynamic performance of passively pitching revolving plates," *AIAA paper 2019-1376,* 2019.

[18] C. Li and H. Dong, "Three-dimensional wake topology and propulsive performance of low-aspect-ratio pitching-rolling plates," *Physics of Fluids,* vol. 28, p. 071901, 2016.

[19] J. Wang, C. Li, Y. Ren, and H. Dong, "Effects of surface morphing on the wake structure and performance of flapping plates," *AIAA paper 2017-3643,* 2017.

[20] C. Li and H. Dong, "Quantification and Analysis of Propulsive Wake Topologies in Finite Aspect-Ratio Pitching-Rolling Plates," *AIAA Paper 2016-4339,* 2016.

[21] M. Xu, M. Wei, C. Li, and H. Dong, "Adjoint-based optimization for thrust performance of three-dimensional pitching–rolling plate," *AIAA Journal,* vol. 57, pp. 3716-3727, 2019.

[22] H. Dong, A. T. Bode-Oke, and C. Li, *Learning from nature: unsteady flow physics in bioinspired flapping flight*: InTech, 2018.

[23] Y. Liu, A. D. Lozano, T. L. Hedrick, and C. Li, "Comparison of experimental and numerical studies on the flow structures of hovering hawkmoths," *Journal of Fluids and Structures,* vol. 107, p. 103405, 2021.

[24] C. Li, J. Jiang, H. Dong, and K. Zhao, "Computational modeling and validation of human nasal airflow under various breathing conditions," *Journal of biomechanics,* vol. 64, pp. 59-68, 2017.

[25] C. Li, J. Jiang, K. Kim, B. A. Otto, A. A. Farag, B. J. Cowart*, et al.*, "Nasal structural and aerodynamic features that may benefit normal olfactory sensitivity," *Chemical senses,* vol. 43, pp. 229-237, 2018.

[26] M. Lei, J. P. Crimaldi, and C. Li, "Navigation in odor plumes: How do the flapping kinematics modulate the odor landscape?," *AIAA 2021-2817,* 2021.

[27] M. Lei and C. Li, "Effects of Wing Kinematics on Modulating Odor Plume Structures in the Odor Tracking Flight of Fruit Flies," *FEDSM 2021-61832,* 2021.

[28] D. Ishihara, Y. Yamashita, T. Horie, S. Yoshida, and T. Niho, "Passive maintenance of high angle of attack and its lift generation during flapping translation in crane fly wing," *Journal of Experimental Biology,* vol. 212, pp. 3882-3891, Dec 2009.

[29] M. Lei and C. Li, "The aerodynamic performance of passive wing pitch in hovering flight," *Physics of Fluids,* vol. 32, p. 051902, 2020.

[30] C. Li, J. Wang, G. Liu, X. Deng, and H. Dong, "Passive pitching mechanism of three-dimensional flapping wings in hovering flight," in *ASME-JSME-KSME 2019*

8th Joint Fluids Engineering Conference, 2019, pp. AJKFluids2019-4639, V002T02A043.

[31] X. Meng, Y. Liu, and M. Sun, "Aerodynamics of ascending flight in fruit flies," *Journal of Bionic Engineering,* vol. 14, pp. 75-87, 2017.